Growth patterns and properties of aerosol-assisted chemical vapor deposition of $CH_3NH_3PbI_3$ films in a single step[1]

Mohammad Afzaal* and Heather M. Yates

Materials and Physics Research Centre, The University of Salford, Salford, M5 4WT, United Kingdom.

E-mail: M.Afzaal@salford.ac.uk

ABSTRACT

In this work, we highlight growth patterns and properties of aerosol-assisted chemical vapor deposition of perovskite, $CH_3NH_3PbI_3$ thin films. The substrates were distinctly covered with both perovskite and lead iodide thin films which we attribute to methylammonium iodide being the rate limiting step via mass transport. The black perovskite films demonstrated strong absorption and photoluminescence properties confirming their suitability as a light absorbing material for the fabrication of solar cells. Scanning electron microscope images showed dense morphologies along with the confirmation of holes and gaps at reduced growth temperature.

Keywords: chemical vapor deposition; perovskite film; tetragonal; photoluminescence; rate limiting step

1. Introduction

Tremendous progress at multiple facets of perovskite (PVK) solar cell technologies has resulted in solar to electrical power conversion efficiencies increasing from 3.8% [1] in 2009 to presently in excess of 23% (for PVK/silicon solar cells) [2]. With a common formula $CH_3NH_3MX_3$ (M = Pb or Sn; X = Cl, Br or I), the absorber layer is sandwiched between different electron and hole transport layers. Attempts to deposit high-quality optoelectronic PVK layers by one or two-step solution processes such as spin coating are widely spread [3,4], although challenging to scale up.

To meet the challenge of industrial scale, cost-effective deposition of dense PVK coatings use of the chemical vapor deposition (CVD) processes would be highly desirable. The atmospheric pressure deposition technique is particularly suited to use in industry due to the high volume, continuous growth processes and fast growth rates achievable. Moreover, the process has already been shown to be cost competitive and capable of integration in manufacturing processes such as the float-glass industry. The technique enables the control of a range of film properties such as thicknesses, morphologies, and growth rates through careful adjustment of the deposition conditions. Various groups have used modified CVD processes for depositing device quality PVK thin films either through vaporisation of organic part alone or organic and inorganic components separately. For example, Qi et al. introduced hybrid CVD through thermal evaporation of lead chloride followed by vapor phase deposition of methylammonium iodide (MAI) [5]. Low-pressure CVD has been shown to produce uniform $CH_3NH_3PbI_3$ absorbing layers by decreasing the over-rapid intercalating reaction rate [6]. However, concerns about the stoichiometry and the thermal stability of the organic part remain relatively large. In addition, use of expensive and complicated vacuum configurations are also likely to have detrimental impact on the versatility and commercialization of large scale deposition of films. Lead being not only cheap, it can also

be easily recycled effectively and economically**.** Although there are issues due to the toxicity of the metal, which has sparked an interest in lead free perovskites with the substitution of tin [7].

As mentioned above, ability to deposit uniform thin films at atmospheric pressure and in a single step are attractive from a practical point of view. O'Brien's group was the first to report a one-step aerosol-assisted (AA) CVD of $CH_3NH_3PbBr_3$ films with a lead:bromine atomic ratio of 1:3 [8]. One key feature was the conversion of the precursor solution to aerosols via a nebulizer, followed by their transport to the reaction chamber by an inert carrier gas. The process relies on judicial choice of solvent(s) to dissolve the precursors. Palgrave and co-workers extended the work to deposit the more active iodide analogue at ambient pressure [9]. Their work gives the characterisation and analysis for one set of deposition parameters, but no discussion on any trends in film characteristics with deposition parameter. In our study, we consider a range of CVD deposition parameters (deposition temperature, substrate placements and precursor delivery) and their effects on the resulting PVK films. In addition we include both photoluminescence (PL) and Raman studies which have not, as far as we are aware, previously been included in analysis of AACVD deposited films. We highlight some distinct growth observations during the attempted deposition of PVK films and some resulting properties that have not been studied previously in CVD experiments.

2. Experimental details

Prior to conducting experiments, 1.1 mm borosilicate glass (Corning Eagle 2000) were cleaned with detergent, water, propan-2-ol, and dried in air. The reasons for using borosilicate glass (2 × 10 cm) as substrates for thin films are thermal stability and enhanced optical properties. Vicks paediatric mini ultrasonic humidifier was used as the nebuliser. Both CH_3NH_3I and $CH_3NH_3PbI_3$ were synthesized according to the reported method [10]. The

nitrogen (N_2) flow rate was controlled using a Platon NGX glass variable area flowmeter. An IEC - type K thermocouple was used to measure the surface temperature of the films.

2.1 Deposition of Thin films: The system was purged under a constant flow rate of N_2 at the required deposition temperature, before carrying out any experiments. After diluting $CH_3NH_3PbI_3$ with dimethylformamide (DMF) (0.153 M), experiments were conducted in a standard electric furnace between 200-275 °C with a constant nitrogen flow rate of 0.5 l/min at atmospheric pressure. After 2 hours of deposition (to allow maximum usage of precursor), substrates were allowed to cool to room temperature (*ca*. 2 hours) under N_2 before being taken out for characterisation. A standard CVD gas delivery system [11] was used with a tubular furnace as the reactor.

2.2 Characterisation: Transmission and reflection were measured using an Aquila nkd 8000 spectrophotometer between 400 and1000 nm at an incident angle of 30° using s polarisation. Scanning electron microscope images were recorded on a XL30 FEG SEM, with sputtered carbon coatings to avoid charging. X-ray diffraction measurements were taken using a Siemen D5000 instrument. The average film thickness was determined using a Dektak 3ST surface profiler by measuring at least five different points across the sample. Photoluminescence and Raman spectroscopic studies were performed as previously reported [12] at an excitation wavelength of 532 nm. Crystallite size was calculated by Scherrer Equation.

$$D = \frac{0.94\lambda}{\beta\cos\theta}$$

3. Results and Discussion

Keeping the PbI_2/MAI molar ratio fixed at 1:1 in DMF, AACVD experiments were performed on 1.1 mm borosilicate glass in a tube furnace. After diluting 1.2 ml aliquot of solution with 12 ml of DMF, experiments were conducted at a range of temperatures for a fixed 2 hour deposition time. To lower the possibility of aerosols condensing within the

delivery tube and to allow efficient mass transport of chemicals, the distance between the deposition area and the precursor outlet was optimized.

To monitor the effect of deposition temperatures (200-275 ^{o}C), preliminary studies focused on the substrates placed in the middle of the furnace i.e. hot zone while keeping all the growth conditions constant (scheme 1). To our surprise, all the films were found to be yellow and their resulting X-ray powder diffraction (XRD) patterns showed only PbI_2 (JCPDS: 80-1000). Black deposits were also found on the reactor walls near the gas inlet, which indicates that the intercalation of $CH_3NH_3^+$ into the PbI_2 is not only temperature sensitive, but that the distance between precursor entry and deposition area is critical [13]. After taking account of these observations, further experiments were conducted by placing the substrates at the upstream entry of the furnace (approx. 4 cm).

At 200 °C, with samples at the new upstream position poor film coverage was observed. This was mainly due to materials being condensed onto sidewalls of the tube, rather than the glass substrate as the actual substrate temperature was too low. Tests established that as well as a temperature gradient along the furnace, the actual substrate temperature was lower than the set point (set temperature: 200-275 °C, actual temperature: 140-255 °C as measured at the new sample position by placing a thermocouple on the top of the substrates). By increasing the growth temperature up to 275 °C, improved surface coverage with distinct black and yellow regions were evident (Fig. 1). The difference in temperature required by Palgrave et al (200 ^{o}C) [9] and ourselves to obtain PVK films is almost certainly due to heating method adopted for the substrate. Use of a cold wall reactor with a flat heated susceptor is more efficient at transferring heat uniformly to the substrate surface, than a hot-wall furnace with the substrate only touching at the edges. In a cold wall reactor, only the substrates are radiatively or inductively heated while keeping the reactor

walls cool. Whereas in a hot-wall furnace, both the substrates and the reactor walls are heated.

Major XRD peaks resulting from the black areas of the substrates confirmed the formation of tetragonal (the room-temperature stable phase) $CH_3NH_3PbI_3$ crystals [14]. Minor but important peaks at 10.68°, 13.04° and 26.36° (marked as * in Fig. 2) could not be assigned to either PbI_2 or MAI and their intensities remain unchanged with increased growth temperatures (Fig. 2). However, these 2θ values match with a recent study by Burda et al. who identified the origin of these peaks from a monoclinic PbI_2-MAI-DMF intermediate complex [15]. This implies that the complete formation of PVK films proceeds via an intermediate which is due to $CH_3NH_3^+$ intercalating into the PbI_2 network during the evaporation of DMF in the furnace. Seok and co-workers have reported a similar intermediate phase of PbI_2-MAI-DMSO (Dimethyl sulfoxide) [16]. One noticeable difference between the resulting XRD patterns of PVK films is that their preferred orientation is temperature dependent (Fig. 2). At temperatures ranging 200-250 ^oC, a preferred orientation along the (110) plane is evident but switches to (202) plane at 275 ^oC. Crystallite sizes estimated using Scherrer's equation range between 31-36 nm. In previous work by AACVD, a preferred orientation of (100) was observed for PVK films [9]. The change is most likely due to the different deposition conditions (temperature and deposition rate) used. The XRD spectra of yellow portion of the substrates was confirmed to be pure PbI_2, with *c*-axis oriented (001) peak at 12.68° (Fig. 2).

The growth of two different materials as evident by the colour change in our experiments appear to suggest that the full conversion of PbI_2 to perovskite was limited by the amount of MAI reaching the substrate surface i.e. MAI was the rate limiting step in mass transport. This would result in a MAI concentration gradient along the reaction tube and lead

to the part of the substrate closest to the precursor inlet being oversaturated, with little or no MAI available for the intercalation further away from the precursor source.

Samples deposited at different temperatures exhibited very different structural features, as demonstrated in the scanning electron microscope images of the black areas (Fig. 3). To illustrate the point, continuous random network structures of MAPI at 200 ^{o}C (Fig. 3a) changed to micron-sized granular structures with large grain boundaries at 250 ^{o}C (Fig. 3b). Both these surface morphologies are regularly found in CVD [9] and solution processing methodologies [17]. Film thicknesses estimated by the surface profilometer were found to be 65 (±10) nm at 200 ^{o}C and 148 (±31) nm at 250 ^{o}C. This results in growth rates of 33 nm/h and 74 nm/h at 200 ^{o}C and 250 ^{o}C, respectively. No appreciable difference in I/Pb atomic ratios of films was detected in energy dispersive X-ray analysis, with values only ranging between 2.4-2.7:1.

Various, sometimes contradictory interpretations of theoretical and experimental Raman vibrational analysis exist for clean PVK thin films [18-20] which may be a consequence of Raman conditions employed. Our Raman spectroscopy results on the black areas of the films at ambient conditions (excitation wavelength (λ_{ex}) 532nm) showed bands at 97, 112, 171 and 220 cm^{-1} attributed to Pb–I bonds and organic cation motions and is consistent with a prior study (Fig. 4) [21]. It is worth remembering that PbI_2 is one of the decomposition by-products of a PVK layer, due to the presence of air moisture [22]. A similar observation has also been noted by Ledinský and co-workers who reported the decomposition even under vacuum conditions [18]. The sample was intentionally heated through an increased laser power from 40% to 70%, which is considerably high for photosensitive materials, to see if it was possible to deduce any further structural distortions or modifications. Two new peaks at 139 and 289 cm^{-1} emerged, whereas the broad band at 171 cm^{-1} vanished. The strong peak at the lower wavenumber peak corresponds to the

liberation of the MA cations [20]. The origin of the unusually broad peak at 287 cm^{-1}, as described by Quarti et al., reflects the torsional mode of the organic cations and points to the increased orientational disorder of the material [20].

The absorption coefficients (α) are determined from the transmission (T), reflection (R) and thickness (t) measurements using $\alpha = -\ln[T/(1-R)]/t$ (Fig. 5a) [23]. The onset of the interband absorption shown in Fig. 5b around 1.63 eV. One noticeable feature in our data is the presence of a large absorption tail (reflecting the peak asymmetry) towards the low energy that could be described in terms of an Urbach tail or possibly scattering caused by the grain boundaries [24]. The deposited films exhibited photoluminescence (PL) properties as demonstrated by the room temperature PL studies (λ_{ex} = 532 nm), which again confirmed the deposition of PVK. A film deposited at 250 °C, gave an emission peak (λ_{em}) at 1.63eV with a full width at half maximum (FWHM) of 79 meV as shown in Fig. 5b. No shift with respect to its absorption was found, in contrary, to energy shifts previously seen for the $CH_3NH_3PbI_3$ system and ascribed to self-absorption [25]. With decreasing deposition temperature, λ_{em} shifts due to phase change from tetragonal to orthorhombic as shown by Sutherland et al [26]. At higher photon energies, the peak shape became slightly asymmetric and reflects the inherent nature of the emitting species [19]. Figure 5c demonstates the shift in energy between samples deposited at different temperatures. We find that the λ_{em} at 200 ^oC (Fig. 5c) was marginally shifted towards lower energy (few meV) due to quantum confinement effects with a larger FWHM (89 meV) which reflects an increased distribution of particle sizes. This is in line with the rather looser film network as seen in the SEM images (Fig. 3a).

4. Conclusions

By control of deposition temperature and substrate position, an AACVD process in a tube furnace has been shown to deposit tetragonal $CH_3NH_3PbI_3$ films. Careful control of sample position relative to the precursor entry point was important to prevent deposition of only PbI_2

films, which occurred due to MAI being the self-limiting step during the process. Although perovskite could be deposited at 200 ^{o}C, the optimum temperature for a more compact film was 250 ^{o}C. The perovskite films exhibited strong absorption and emission properties, suggesting their suitability as light absorbing materials for the fabrication of solar cell devices. Raman spectroscopy showed bands assigned to PbI_2 and organic components which are decomposition products of perovskite films. The enhanced presence of the PbI_2 may be induced by the intensity of the excitation laser.

Acknowledgements

This work was financed by EU Horizon 2020 grant H2020-LCE-2015-16-53296 CHEOPS Highly Efficient photovoltaic Perovskite Solar cells. We would like to thank Dr John E Proctor and Hakeem Malik (University of Salford) for their help with the photoluminescence and Raman studies.

References

[1] A. Kojima, K. Teshima, Y. Shirai, T. Miyasaka, Organometal halide perovskites as visible-light sensitizers for photovoltaic cells, J. Am. Chem. Soc. 131 (2009) 6050.

[2] K.A. Bush, A.F. Palmstrom, Z.J. Yu, M. Boccard, R. Cheacharoen, J.P. Mailoa, D.P. McMeekin, R.L.Z. Hoye, C.D. Bailie, T. Leijtens, I.M. Peters, M.C. Minichetti, N. Rolston, R. Prasanna, S. Sofia, D. Harwood, W. Ma, F. Moghadam, H.J. Snaith, T. Buonassisi, Z.C. Holman, S.F. Bent, M.D. McGehee, 23.6%-efficient monolithic perovskite/silicon tandem solar cells with improved stability, Nature Energy, 2 (2017) 17009.

[3] M.M. Lee, J. Teuscher, T. Miyasaka, T.N. Murakami, H.J. Snaith, Efficient hybrid solar cells based on meso-superstructured organometal halide perovskites, Science, 338 (2012) 643.

[4] C. Zuo, H.J. Bolink, H. Han, J. Huang, D. Cahen, L. Ding, Advances in perovskite solar cells, Adv. Sci. 3 (2016) 1500324.

[5] M.R. Leyden, L.K. Ono , S.R. Raga , Y. Kato , S. Wang , Y. Qi , High performance perovskite solar cells by hybrid chemical vapor deposition, J. Mater. Chem. A 2 (2014) 18742 .

[6] P. Luo , Z. Liu , W. Xia , C. Yuan , J. Cheng , Y. Lu , Uniform, stable, and efficient planar-heterojunction perovskite solar cells by facile low-pressure chemical vapor deposition under fully open-air conditions, ACS Appl. Mater. Interfaces 7 (2015) 2708.

[7] N.K. Noel, S.D. Stranks, A. Abate, C. Wehrenfennig, S. Guarnera, A.-A. Haghighirad, A. Sadhanala, G.E. Eperon, S.K. Pathak, M.B. Johnston, A. Petrozza, L.M. Herz, H.J. Snaith, Lead-free organic–inorganic tin halide perovskites for photovoltaic applications, Energy Environ. Sci. 7 (2014) 3061.

[8] D.J. Lewis, P. O'Brien, Ambient pressure aerosol-assisted chemical vapour deposition of $(CH_3NH_3)PbBr_3$, an inorganic–organic perovskite important in photovoltaics Chem. Commun. 50 (2014) 6319.

[9] D.S. Bhachu, D.O. Scanlon, E.J. Saban, H. Bronstein, I.P. Parkin, C.J. Carmalt, R.G. Palgrave, Scalable route to $CH_3NH_3PbI_3$ perovskite thin films by aerosol assisted chemical vapour deposition, J. Mater. Chem. A 3 (2015) 9071.

[10] S. Aharon, B.E. Cohen, L. Etgar, Hybrid lead halide iodide and lead halide bromide in efficient hole conductor free perovskite solar cell, J. Phys. Chem C 118 (2014) 17160.

[11] G.A. Horley, M.R. Lazell, P. O'Brien, Deposition of thin films of gallium sulfide from a novel liquid single-source precursor, $Ga(SOCNEt_2)_3$, by aerosol-assisted CVD, chem. vap. deposition 5 (1999) 205.

[121] D. Smith, R.T. Howie, I.F. Crowe, C.L. Simionescu, C. Muryn, V. Vishnyakov, K.S. Novoselov, Y.-J. Kim, M.P. Halsall, E. Gregoryanz, J.E. Proctor, Hydrogenation of graphene by reaction at high pressure and high temperature, ACS Nano 9 (2015) 8279.

[13] M.R. Leyden, M.V. Lee, S.R. Raga, Y. Qi, Large formamidinium lead trihalide perovskite solar cells using chemical vapor deposition with high reproducibility and tunable chlorine concentrations, J. Mater. Chem. A 3 (2015) 16097.

[14] T. Oku, 'Crystal structures of $CH_3NH_3PbI_3$ and related perovskite compounds', in solar Cells - new approaches and reviews, Ed. L.A. Kosyachenko, ISBN 978-953-51-2184-8, Publisher: In Tech, 2015, pp77-101.

[15] X. Guo, C. McCleese, C. Kolodziej, A.C.S. Samia, Y. Zhao, C. Burda, Identification and characterization of the intermediate phase in hybrid organic–inorganic $MAPbI_3$ perovskite**,** *Dalton Trans*. 45 (2016) 3806.

[16] N.J. Jeon, J.H. Noh, Y.C. Kim, W.S. Yang, S. Ryu, S.I. Seok, Solvent engineering for high-performance inorganic–organic hybrid perovskite solar cells, Nat. Mater. 13 (2014) 897.

[17] Y. Zhang, J. Du, X. Wu, G. Zhang, Y. Chu, D. Liu, Y. Zhao, Z. Liang, J. Huang, Ultrasensitive photodetectors based on island-structured $CH_3NH_3PbI_3$thin films, ACS Appl. Mater. Interfaces 7 (2015) 21634.

[18] M. Ledinský, P. Löper, B. Niesen, J. Holovský, S.-J. Moon, J.-H. Yum, S. De Wolf, A. Fejfar, C. Ballif, Raman spectroscopy of organic–inorganic halide perovskites, J. Phys. Chem. Lett. 6 (2015) 401.

[19] G. Grancini, S. Marras, M. Prato, C. Giannini, C. Quarti, F. De Angelis, M. De Bastiani, G.E. Eperon, H.J. Snaith, L. Manna, A. Petrozza, The impact of the

crystallization processes on the structural and optical properties of hybrid perovskite films for photovoltaics, J. Phys. Chem. Lett. 5 (2014) 3836.

[20] C. Quarti, G. Grancini, E. Mosconi, P. Bruno, J.M. Ball, M.M. Lee, H.J. Snaith, A. Petrozza, F. De Angelis, The Raman spectrum of the $CH_3NH_3PbI_3$ hybrid perovskite: interplay of theory and experiment, J. Phys. Chem. Lett. 5 (2014) 279.

[21] X. Liu, L. Niu, C. Wu, C. Cong, H. Wang, Q. Zeng, H. He, Q. Fu, W. Fu, T. Yu, C. Jin, Zheng Liu, T. C. Sum, Periodic organic–inorganic halide perovskite microplatelet arrays on silicon substrates for room-temperature lasing, Adv. Sci. 3 (2016) 1600137.

[22] J.M. Frost, K.T. Butler, F. Brivio, C.H. Hendon, M. van Schilfgaarde, A. Walsh, Atomistic origins of high-performance in hybrid halide perovskite solar cells, Nano Lett. 14 (2014) 2584.

[23] E.T. Hoke, D.J. Slotcavage, E.R. Dohner, A. R. Bowring,H.I. Karunadasa, M.D. McGehee, Reversible photo-induced trap formation in mixed halide hybrid perovskites for photovoltaics, Chem. Sci. 6 (2015) 613.

[24] Y. Yamada, T. Nakamura, M. Endo, A. Wakamiya Y. Kanemitsu, Near-band-edge optical responses of solution-processed organic–inorganic hybrid perovskite $CH_3NH_3PbI_3$ on mesoporous TiO_2 electrodes, Appl. Phys. Express 7 (2014) 032302.

[25] M. Saba, M. Cadelano, D. Marongiu, F. Chen, V. Sarritzu, N. Sestu, C. Figus, M. Aresti, R. Piras, A.G. Lehmann, C. Cannas, A. Musinu, F. Quochi, A. Mura, G. Bongiovanni, Correlated electron–hole plasma in organometal perovskites, Nat. Commun. 5 (2014) 5049.

[26] B.R. Sutherland , S. Hoogland , M.M. Adachi , P. Kanjanaboos, C.T.O. Wong , J.J. McDowell , J. Xu , O. Voznyy , Z. Ning , A. J. Houtepen, E. H. Sargent, Perovskite thin films via atomic layer deposition, Adv. Mater. 27 (2014) 53.

Figure captions

Scheme 1. Schematic illustration showing substrate positions in the tube reactor during the coating experiments.

Fig. 1. A photograph showing as-deposited film at 275 ^{o}C.

Fig. 2. XRD patterns of tetragonal $CH_3NH_3PbI_3$ and hexgonal PbI_2 deposited at different temperatures. * indicate monoclinic PbI_2-MAI-DMF intermediate.

Fig. 3. SEM images of deposited films at 200 ^{o}C and 250 ^{o}C temperatures.

Fig. 4. Raman spectra of film deposited at 250 °C with different laser powers.

Fig. 5. (a) Transmission and reflection spectra, and (b) absorption coefficient and photoluminescence of films deposited at 250 °C. (c) Photoluminescence spectra of deposited perovskite thin films at different growth temperatures.

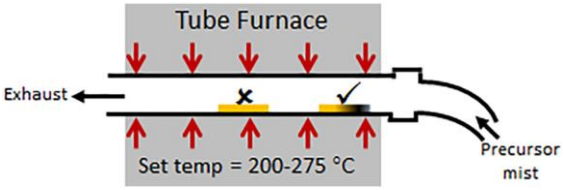

schematic

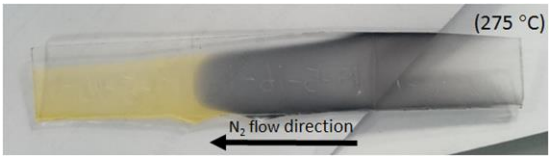

Fig.1

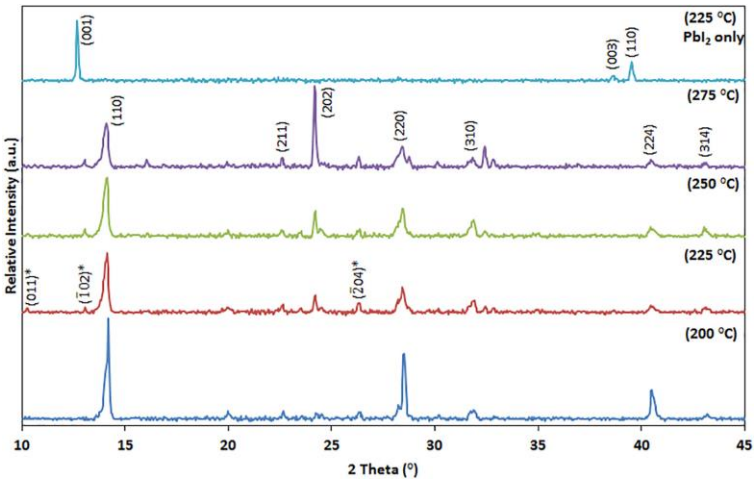
(225 °C)
PbI2 only
(001)
(003)
(110)
(275 °C)
(110)
(211)
(202)
(220)
(310)
(224)
(314)
(250 °C)
(225 °C)
(011)*
(1̄02)*
(2̄04)*
(200 °C)
Relative Intensity (a.u.)
10
15
20
25
30
35
40
45
2 Theta (°)

Fig.2

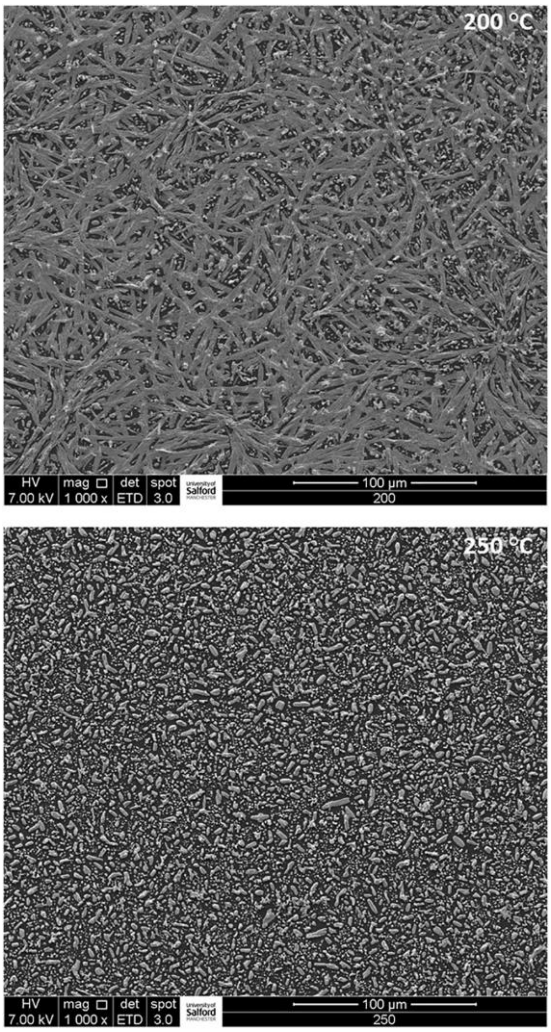
200 °C
HV
7.00 kV
mag
1 000 x
det
ETD
spot
3.0
100 µm
200
250 °C
HV
7.00 kV
mag
1 000 x
det
ETD
spot
3.0
100 µm
250

Fig.3

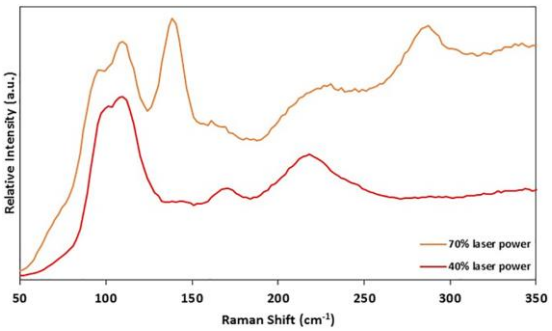
Relative Intensity (a.u.)
70% laser power
40% laser power
50
100
150
200
250
300
350
Raman Shift (cm-1)

Fig.4

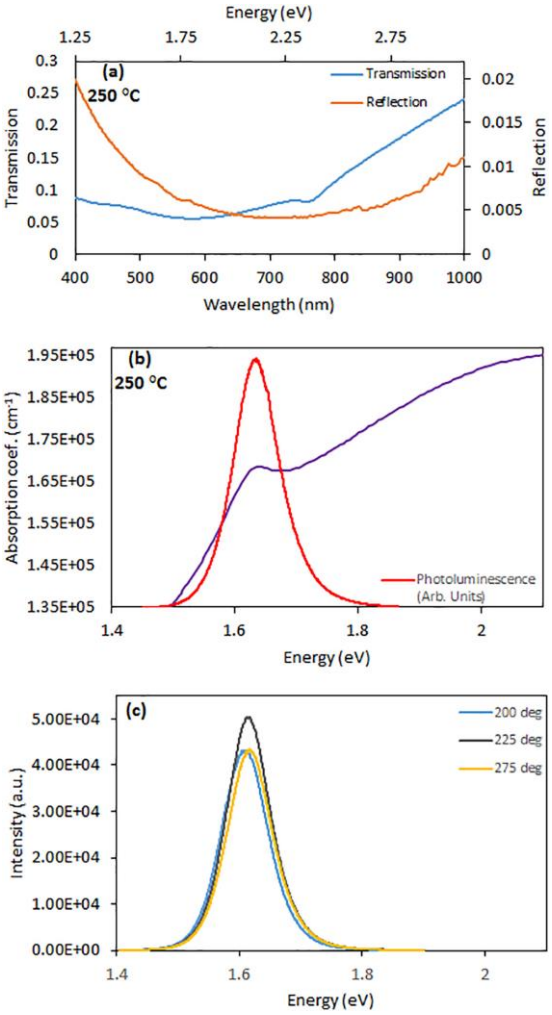
Energy (eV)
1.25
1.75
2.25
2.75
(a)
250 °C
Transmission
Reflection
Transmission
Reflection
Wavelength (nm)
(b)
250 °C
Photoluminescence (Arb. Units)
Absorption coef. (cm-1)
Energy (eV)
(c)
200 deg
225 deg
275 deg
Intensity (a.u.)
Energy (eV)

Fig.5